Uniaxial Magnetic Anisotropy of $L1_0$-FeNi Films with Island Structures on $LaAlO_3$ (110) Substrates by Nitrogen Insertion and Topotactic Extraction*

Takahiro NISHIO Keita ITO Hiroaki KURA
Koki TAKANASHI Hideto YANAGIHARA

Tetrataenite ($L1_0$-FeNi) has potential for application in next-generation permanent magnets. This compound is a rare-earth-free material comprising Fe and Ni, which are abundant elements. In addition, an extremely high uniaxial magnetocrystalline anisotropy (K_u) is expected for $L1_0$-FeNi because of the ordered arrangement of the elements. This study reports the magnetic properties of uniaxially oriented $L1_0$-FeNi films with island structures fabricated by a novel method involving the radio-frequency sputter deposition of FeNi alloy films onto a $LaAlO_3$(LAO)(110) substrate, followed by nitrogen insertion and topotactic extraction. The uniaxial magnetic anisotropy of the $L1_0$-FeNi films is determined from the magnetization curves via magnetic torque measurements of the films. The obtained $L1_0$-FeNi film exhibiting a relatively high superlattice order parameter of 0.74 yielded K_u of ˜0.63 MJ/m^3, as well as coercivities of 319 kA/m at 300 K. This coercivity is the highest value reported for artificial $L1_0$-FeNi to date.

Key words :
Magnetic films, Nanostructured materials sputter deposition, Nitriding, Superlattice, Magnetocrystalline anisotropy

1. Introduction

The demand for rare-element-free permanent magnets, which are ubiquitous in electric vehicles, robotics, wind power generation, and storage devices in consumer electronics and home appliances, is increasing because of the trend toward a carbon-neutral and a more sustainable society. $L1_0$-FeNi is a promising material for meeting the demand because it does not contain noble metals or rare-earth elements. The high potential of $L1_0$-FeNi as a magnetic material is attributed to its crystal structure that has alternately stacking monatomic layers of Fe and Ni along the c-axis [1)-5)]. According to a previous study [4)], the substantial magnetic anisotropy energy in $L1_0$-FeNi is primarily attributed to the spin–orbit interaction with the orbital anisotropy in 3d Fe electrons owing to the $L1_0$ structural ordering, as was revealed by X-ray magnetic circular dichroism measurements. This result agrees with the prediction made through a first-principles calculation [5)]. $L1_0$-FeNi sometimes partly exists in some meteorites because the structural transformation temperature of the compound is so low that the structural ordering process takes an extremely long time owing to the very low atomic diffusion velocity. Studies of $L1_0$-FeNi phases have revealed a high uniaxial magnetocrystalline anisotropy energy (K_u) of 0.84 MJ/m^3 [6)], as well as high coercivity (H_c) values of 100–796 kA/m [7)-9)]. Moreover, methods for synthesizing artificial bulk $L1_0$-FeNi by the neutron irradiation of disordered FeNi alloy (A1-FeNi) in a magnetic field have been reported; these methods yield a K_u value of ˜1.3 MJ/m^3 [10)11)].

Recently, several industrially compatible synthetic methods have been proposed. The nitrogen insertion and topotactic extraction (NITE) process is a method to promote the ordering of Fe and Ni using the tetragonal FeNiN phase, which is an anti-ferromagnet with a N´eel temperature of 178 K possessing an ordered Fe and Ni structure similar to $L1_0$-FeNi [12)-14)]. By nitriding A1-FeNi powders with ammonia gas and denitriding with hydrogen, $L1_0$-FeNi powders that have a high long-range order (S) of 0.71 and an H_c of 142 kA/m have been produced [14)]. Moreover, a mechanical alloying process to obtain $L1_0$-FeNi powders has been reported; this process yields an S of 0.3 [15)]. Further, a third element such as P has been added to FeNi, and an $L1_0$-ordered structure has been synthesized [16)]. Despite these synthetic attempts, larger K_u and H_c values than those of meteorites or neutron-irradiated $L1_0$-FeNi are yet to be achieved.

As an alternative to bulk production methods, molecular beam epitaxy (MBE) has been used to achieve high magnetic anisotropy in FeNi films. In this process, Fe and Ni monolayers are deposited alternately, yielding S = 0.48 and K_u = 0.7 MJ/m^3 [17)]. Another approach is to grow epitaxial FeNiN(100) films on MgO(001), $MgAl_2O_4$(001), and $SrTiO_3$ (STO)(001) substrates and to subsequently convert them to epitaxial $L1_0$-FeNi (100) films by denitriding [18)]. The highest S of 0.87 was obtained for $L1_0$-FeNi(100)/STO(001); however, the film had two types of nanoscale crystallographic variants with the c-axes of each variant intersecting at 90°, and K_u was suppressed to 0.59 MJ/m^3 because of the competition of the uniaxial magnetic anisotropy of each variant [19)]. Therefore, to obtain a reliable value of K_u, the $L1_0$-FeNi films should be uniform and free of variants. For $L1_0$-FeNi films on $LaAlO_3$ (LAO)(110) substrates, the two-fold symmetry of the LAO(110) surface allows the growth of variant-free epitaxial $L1_0$-FeNi(110) films, yielding S = 0.60 and K_u = 0.55 MJ/m^3 [20)]. However, their H_c is not large (˜95 kA/m) because the magnetic domain walls move smoothly in these uniform films.

To enhance H_c, it is important to form single magnetic domain particles with easy magnetization axes arranged coherently according to the Stoner-Wohlfarth (SW) theoretical model [21)]. One method to achieve this is the formation of films by sputtering, which yields isolated island structures [22)23)]. Island-shaped $L1_0$-FeNi thin films on quartz glass substrates have been formed by applying the NITE process to the sputtered films; these films have an even higher H_c of ˜188 kA/m [23)]. However, the system is not appropriate to obtain the maximized H_c predicted by SW model because the easy magnetization axes of the islands are randomly oriented. Moreover, the K_u value has not been measured, and therefore, it is difficult to derive the potential H_c value. In this study, highly oriented and $L1_0$-ordered FeNi films with sufficiently isolated island structures that can be considered as SW-type particles were fabricated on an LAO(110) substrate using the NITE method. This study aims to measure the maximized H_c and

* This article was published in Journal of Alloys and Compounds, 976, Takahiro Nishio, Keita Ito, Hiroaki Kura, Koki Takanashi, Hideto Yanagihara, Uniaxial magnetic anisotropy of $L1_0$-FeNi films with island structures on $LaAlO_3$ (110) substrates by nitrogen insertion and topotactic extraction, 172992, Copyright Elsevier (2024).

K_u values directly in these $L1_0$-FeNi films with island structures and compare the orientation and S of the film quantitatively for investigating the potential H_c of synthetic $L1_0$-FeNi. As the NITE method is suitable for industrial applications, we believe that this study holds considerable significance in determining the potential for the future scale-up of $L1_0$-FeNi magnetic powder synthesis with high degree of order.

2. Experimental

2.1 Film deposition and NITE

The $L1_0$-FeNi films were fabricated on LAO(110) using sputter deposition and the NITE method, as shown in Fig. 1. First, A1-FeNi films were deposited by the magnetron sputtering of FeNi alloy targets (Kojundo Chemical Laboratory Co., Ltd., Fe:Ni=50:50 at%, 99.99% purity) onto LAO(110) substrates using a high vacuum (base pressure <2.0 × 10^{-5} Pa) radio-frequency (RF) sputtering system (CMS-6420, COMET Corp.). The substrates were held at 400 ℃ under a pressure of 0.3 Pa with a flow of high-purity argon (purity 6 N) during the RF sputtering deposition. The nominal growth rate was around 0.5-0.6 nm/min. The thickness of the film was controlled by varying the deposition time. The average thicknesses of the films after deposition and the subsequent NITE process are 12.4 ± 0.6, 16.8 ± 0.7, and 17.2 ± 0.8 nm for samples denoted A, B, and C, respectively, as listed in Table 1.

The nitriding and denitriding processes were as follows. The sputter deposited films with a size of approximately 4 × 4 mm^2 were placed in an electric furnace. In an atmosphere of ammonia gas (purity 5 N), which flowed through the tube at a rate of 5 L/min, the samples were heated at 325 °C for 20 h. Subsequently, samples A and B were annealed at 375 °C for 10 h and sample C for 1 h. The denitriding process for all samples was conducted in H_2 gas (purity 5 N) flown through the system at a rate of 2 L/min at 200 °C for 2 h.

2.2 Material characterization

The nanostructures of the denitrided films were characterized by scanning electron microscopy (SEM) and transmission electron microscopy (TEM). To examine the topographic structures, planar views of the films were obtained using SEM (JSM-7100F, JEOL). SEM observations were performed at an accelerating voltage of 1.5 kV. A TEM (JEM-ARM300F, JEOL) microscope was used to confirm the $L1_0$-ordering using the fast Fourier transform (FFT) analysis of the TEM images, and the electron diffraction patterns were indexed to the known crystal structures using ReciPro [24]. High-angle annular dark-field scanning TEM (HAADF-STEM) observations and energy dispersive X-ray spectroscopy (EDS) measurements were performed to confirm the composition of the local FeNi films. Before the TEM measurements, all TEM specimens in a cross-sectional geometry were prepared from the film samples using focused-ion-beam (FIB) milling. All observations were performed at an accelerating voltage of 300 kV.

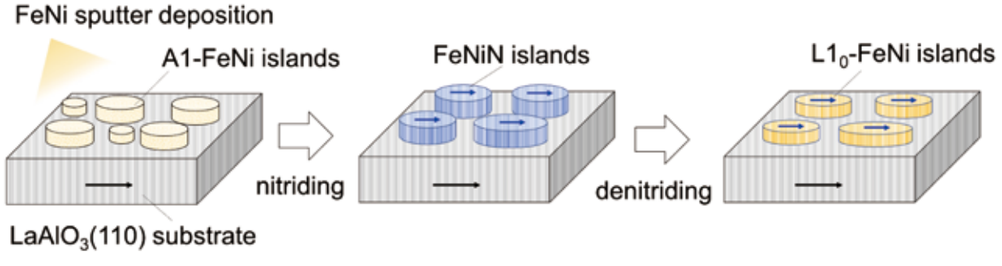

Fig. 1 Fabrication of uniaxial $L1_0$-FeNi(110)/LAO(110) films with island structures. The schematic shows the steps of depositing and forming the $L1_0$-FeNi(110) film on the LAO(110) substrate. The blue and black arrows indicate the [001] direction of each material

The composition and crystal orientations of the FeNi and FeNi-nitride films were analyzed using out-of-plane and in-plane X-ray diffractometry (XRD) using a SmartLab diffractometer (Rigaku Corp.) equipped with a Cu-Kα X-ray radiation source. The visualization for electronic and structural analysis (VESTA) was used to calculate the diffraction peak intensity from the crystal lattice parameters and to draw images of the atomic model [25]. To measure the average thickness of the film, X-ray fluorescence spectroscopy (XRF) analysis was performed using M4 TORNADO (Bruker) assuming the film consists of $L1_0$-FeNi whose density is 8.2 g/cm^3. The average thickness of the film obtained by XRF measurements was calibrated using the values of the continuous FeNi film determined by X-ray reflectivity (XRR) measurements and TEM observations in the cross-sectional direction. To estimate the $L1_0$-ordering of the films after NITE, they were subjected to in-plane XRD measurements on the BL13XU and BL46XU beamlines at the SPring-8 synchrotron radiation facility in Japan. An X-ray energy of 6.90 keV (close to the Fe K absorption edge) was employed in these experiments.

The magnetization curves at 300 K were measured using a vibrating sample magnetometer (VSM) (TM-VSM2614HGCKIT, Tamakawa Co., Ltd.) with a maximum magnetic field sweep of ±2230 kA/m. The magnetic field sweep rate was 8 kA/(m·s) (< 398 kA/m) and 16 kA/(m·s) (≥ 398 kA/m). Further, a magnetic property measurement system (MPMS3, Quantum Design Inc.) equipped with a superconducting magnet was used for magnetization curve measurements at 10 K from −3980 to +3980 kA/m. The K_u values of the films were determined using a torque magnetometer under a 7162 kA/m in-plane field at 300 K using a torque-lever chip mounted on a rotator in a physical property measurement system (PPMS, Quantum Design Inc.).

3. Results and discussion

The typical topographic structure of sample A after the denitriding process is shown in in Fig. 2(a). An island-shaped film with an average island size of 48 ± 12 nm is shown in the planar view of the SEM image, although some islands are partially connected to each other. From the SEM image, the coverage of FeNi is measured to be ~75%. Consequently, the average island thickness is estimated to be 16.5 nm considering the average thickness of 12.4 nm measured via XRF analysis. Fig. 2(b) presents a cross-sectional TEM image of sample A along the [1$\bar{1}$0] axis, revealing islands with a flattened granular structure and a maximum island thickness of ~20 nm. Fig. 2(c) shows an FFT image of the area enclosed by the dotted line on the left island in Fig. 2(b), and superlattice spots within the yellow dotted line can be clearly seen. The pattern matches the expected pattern of epitaxially grown $L1_0$-FeNi(110) on LAO(110) along the [001] axis, as reported by Uehara *et al.*[8]. Therefore, the formation of superlattice structures in the film was confirmed. The STEM/EDS images of the same area are shown in Fig. 2(d)–(j). The composition in the squared area surrounded by the blue dashed line in Fig. 2(d) is Fe 49.2 ± 1.9 at%, Ni 49.3 ± 2.1 at%, La 0.6 ± 0.3 at%, and Al 0.9 ± 0.4 at%, and those of N and O are below the detection limit of 0.1 at%. The nitrogen signal was at the background level, indicating that the denitriding process of the films were fully completed. Although a smaller amount of La and Al than that of FeNi (approximately 1 at%) was detected in the films, the degree of atomic diffusion to the $L1_0$-FeNi islands from the LAO substrate was low, even considering possible contamination because of the FIB milling process to make a TEM specimen. An

特集

oxide layer with a thickness of approximately 2 nm was observed on the FeNi island surface because the sample was exposed to air after the denitriding process, as indicated by the red arrow in Fig. 2(h).

As shown in Fig. 3, XRD measurements are conducted after the nitriding and denitriding of sample A to investigate the crystal orientations of the films over the whole sample area. In the XRD pattern of the sample after nitriding obtained in the out-of-plane configuration (Fig. 3(a)), the peaks were observed at approximately 2θ = 66° and 70°, and these can be assigned to FeNiN 220 and LAO 220, respectively[12) 26)]. The diffraction peak positions of both cubic Fe_2Ni_2N 220 and tetragonally ordered Fe_2Ni_2N 220 overlap with those of LAO 220[12)27)]. However, the existence or absence of ferromagnetic Fe_2Ni_2N phases can be identified based on the observation of the spontaneous magnetization because the FeNiN phase shows paramagnetism at 300 K[12)13)27)]. A nitride film fabricated under the same nitriding conditions as sample A showed no spontaneous magnetization, as confirmed by a magneto-optical Kerr effect measurements, and therefore, sample A is not considered to contain any ferromagnetic Fe_2Ni_2N phases.

Here, the epitaxial relationship between the FeNiN film and the LAO(110) substrate is discussed. There are two types of possible FeNiN variants, as illustrated in Fig. 4. Fig. 4 (a) shows the atomic structure model with the FeNiN(110) and FeNiN(101) planes. The two types of variants grow each direction. The FeNiN(110)-oriented variant shown in Fig. 4(b) exhibits the *c*-axis of FeNiN in the LAO(110) plane and uniaxial crystallinity. In contrast, the FeNiN(101)-oriented variant shown in Fig. 4(c) has a *c*-axis tilted at 47.15° to the LAO(110) and two degrees

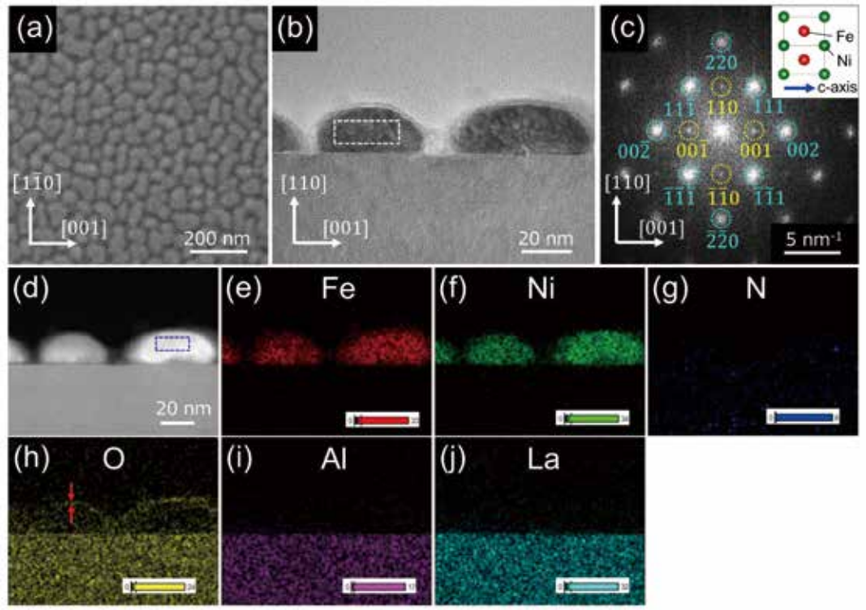

Fig. 2 Morphology and structure of sample A. (a) Planar-view SEM image of sample A, showing the island structures of $L1_0$-FeNi(110). (b) Cross-sectional TEM image of sample A along the [110] axis, showing the epitaxial relationship between $L1_0$-FeNi(110) and LAO(110). (c) FFT image of the squared area surrounded by white dashed line in (b)), showing the diffraction pattern of $L1_0$-FeNi(110). Inset shows the atomic structure model of $L1_0$-FeNi along the [110] axis, which is consistent with the FFT image. (d) Cross-sectional HAADF-STEM image of the same islands in (b), showing the contrast between $L1_0$-FeNi and LAO. (e)–(j) EDS maps for the same area as that in (d), showing the elemental distribution of Fe, Ni, N, O, Al, and La

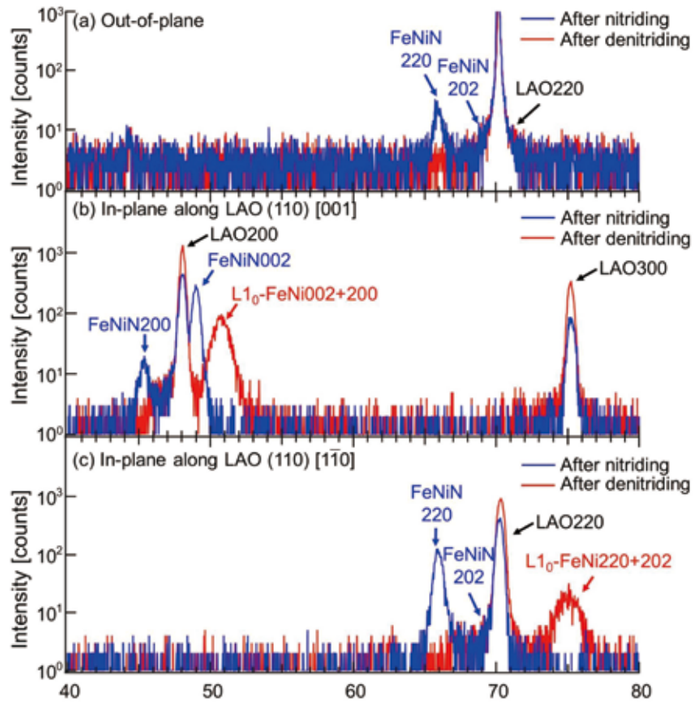

Fig. 3 Cu-Kα XRD patterns of sample A after nitriding and denitriding. (a) Out-of plane and (b) In-plane configurations along LAO(110) [001]; (c) In-plane along LAO(110) [110]. Peaks corresponding to $L1_0$-FeNi, FeNiN, and LAO are labeled

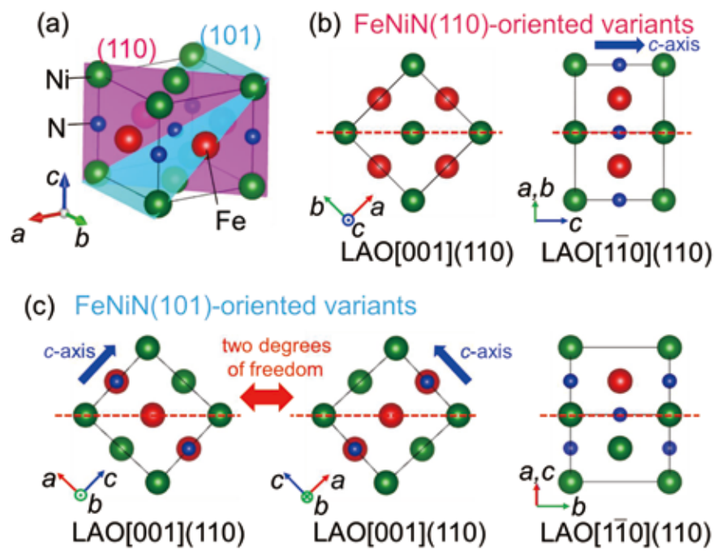

Fig. 4 Crystallographic variants of FeNiN. (a) FeNiN atomic structure model, (b) FeNiN(110)-oriented variant, and (c) FeNiN(101)-oriented variant. The red dashed lines indicate the parallel plane to the LAO(110) substrate

of freedom with respect to the *c*-axis. Therefore, the growth of FeNiN(110)-oriented variants is desirable for obtaining uniaxial crystallinity. In Fig. 3(a), it is difficult to confirm FeNiN(110)-oriented epitaxial growth without FeNiN(101)-oriented variants by using out-of-plane XRD measurements because the FeNiN 202 peak near $2\theta_x = 69°$ is close to that of LAO 220. In-plane XRD measurements were performed to estimate the orientation of growth and crystallographic variants. The results for the incident X-rays along the LAO(110) [001] and LAO(110) [1$\bar{1}$0] directions are shown in Fig. 3(b) and Fig. 3(c), respectively. In Fig. 3(b), the main peak after nitriding originates from FeNiN 002, indicating that the nitrided film includes FeNiN(110)-oriented variants (Fig. 4(b)), and the *c*-axis is parallel to LAO(110) [001]. In Fig. 3(b), a small fraction of FeNiN 200 is also observed. Considering that there are no detectable diffraction peaks except for FeNiN 220 and FeNiN 202 in Fig. 3(c), the result indicates the formation of the FeNiN(101)-oriented variants (Fig. 4(c)). Assuming the topotactic denitriding process of the FeNiN(101)-oriented variants, $L1_0$-FeNi(101)-oriented variants are formed, and the *c*-axis is tilted against the LAO(110) plane.

The volume fraction of variants in the films were estimated quantitatively because the coexistence of variants with the intersecting *c*-axes results in the reduction of the macroscopic K_u[19]. The volume fraction of the FeNiN(110)-oriented variants, P_N, was evaluated using

$$P_N = \frac{I^{obs}_{FeNiN200}}{I^{cal}_{FeNiN200}} \Big/ \left(\frac{I^{obs}_{FeNiN200}}{I^{cal}_{FeNiN200}} + \frac{I^{obs}_{FeNiN002}}{I^{cal}_{FeNiN002}} \right) \times 100\%, \quad (1)$$

where $I^{obs}_{FeNiN200}$ and $I^{obs}_{FeNiN002}$ represent the integrated intensities of the observed diffraction peaks in the $2\theta_x$ direction, whereas $I^{cal}_{FeNiN200}$ and $I^{cal}_{FeNiN002}$ represent the intensities calculated assuming that the orientation of the film is random. The P_N of sample A was estimated to be 96%, indicating that the *c*-axis of FeNiN was highly oriented along LAO(110)[001]. Despite the distinct lack of alignment in the island shape observed in the SEM image of Fig. 2(a), the epitaxial film growth was confirmed via XRD measurements. The obtained P_N values for all films are summarized in Table 1. All samples show $P_N \geq 90\%$, and therefore, the formation of FeNiN(110)-oriented variants on LAO(110) is favorable. Moreover, when comparing samples B and C with nearly identical thicknesses but subjected to varying durations of annealing at 375 °C in an ammonia gas atmosphere, it is evident that an increase in annealing time leads to an improvement in P_N. This suggests that annealing at 375 °C in ammonia gas effectively reduces the volume fraction of FeNiN(101)-oriented variants. In the TEM image of sample A, the $L1_0$-FeNi (110)-oriented variant is mainly observed, whereas the $L1_0$-FeNi (101)-oriented variant is not clearly seen, probably due to the small volume fraction. Further observations are necessary to elucidate the growth mode of crystallographic variants and achieve the formation of a film comprising a single $L1_0$-FeNi (110)-oriented variant.

XRD measurements using anomalous X-ray diffraction near Fe *K* absorption edge were employed to evaluate the *S* values of the films. Fig. 5 shows the results of XRD measurements of the in-plane configuration of sample A. An $L1_0$-FeNi 001 peak was observed, confirming $L1_0$-ordering. *S* is calculated using [17)19)20)]

$$S = \sqrt{\frac{I^{obs}_{L1_0FeNi001} / I^{obs}_{L1_0FeNi002}}{I^{cal}_{L1_0FeNi001} / I^{cal}_{L1_0FeNi002}}}, \quad (2)$$

where $I^{obs}_{L1_0FeNi001}$ and $I^{obs}_{L1_0FeNi001}$ are the integrated intensities of the observed diffraction peaks for $L1_0$-FeNi 001 (superlattice) and $L1_0$-FeNi 002 (fundamental), respectively. $L1_0$-FeNi 002 cannot be distinguished from $L1_0$-FeNi 200 experimentally because the difference of the diffraction peak positions in 2θ between the $L1_0$-FeNi 002 and 200 is less than 0.01°

Table 1 Summary of average thickness, annealing time, P_N, *S* of samples A-C characterized by XRF and XRD measurements

	Average thickness [nm]	Annealing time [h]	P_N	*S*
A	12.4 ± 0.6	10	0.96	0.74
B	16.8 ± 0.7	10	0.96	(0.80)
C	17.2 ± 0.8	1	0.90	(0.60)

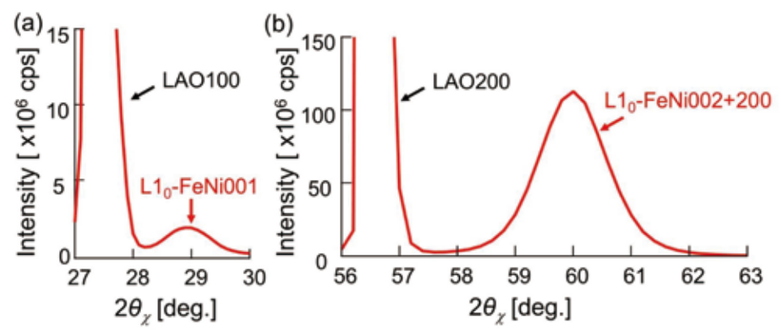

Fig. 5 XRD patterns along LAO [001](110) in sample A using synchrotron radiation (E = 6.90 keV, λ =0.1797 nm) in sample A. (a) Around the superlattice peak of $L1_0$-FeNi 001 and (b) around the peak of $L1_0$-FeNi 002. The peaks corresponding to $L1_0$-FeNi, FeNiN, and LAO are labeled

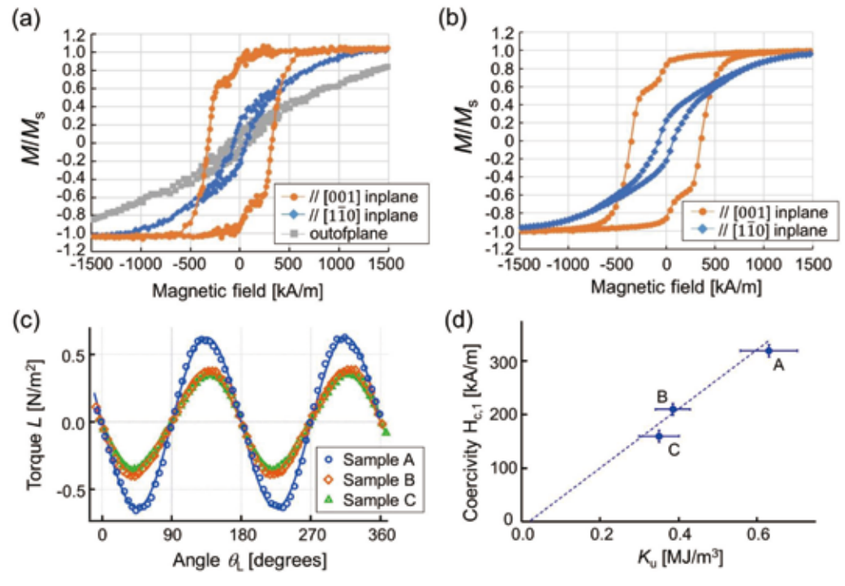

Fig. 6 Magnetic properties of the fabricated $L1_0$-FeNi films. (a) Out-of-plane and in-plane magnetization curves of sample A at 300 K. (b) In-plane magnetization curves of sample A at 10 K. (c) Torque as a function of the angle in the film plane. (d) Plot of $H_{c,1}$ vs. K_u showing a linear relationship

特集

(see Fig. 5(b)). Thus, assuming topotactic nitrogen extraction from the FeNiN(110)- and FeNiN(101)-oriented variants, $I^{obs}_{L1_0FeNi002}$ was estimated from the experimentally measured integrated intensity $I^{obs}_{L1_0FeNi200+002}$ using

$$I^{obs}_{L1_0FeNi002} = \frac{P_N I^{cal}_{L1_0FeNi002}}{(1-P_N) I^{cal}_{L1_0FeNi200} + P_N I^{cal}_{L1_0FeNi002}} I^{obs}_{L1_0FeNi200+002}. \quad (3)$$

For sample A, S was found to be 0.74 using Eq. (3), which is higher than that of a continuous $L1_0$-FeNi(110)/LAO(110) film (S = 0.60) [20]. These results are attributed to the subsequent high-temperature annealing process. Table 1 lists the estimated S values for samples B and C as reference values. Nitrogen residue on the islands were also detected by EDS analysis in sample B, and the S value was slightly overestimated because we did not consider the contributions from the Fe_2Ni_2N phases that overlapped with those of LAO 200 in the calculation of $I^{obs}_{L1_0FeNi002}$. However, assuming a fixed nitrogen residue under the same denitriding condition, the S values of the films were improved by the annealing process.

The magnetic properties of these almost variant-free and highly oriented $L1_0$-FeNi films are discussed. Fig. 6(a) shows the magnetization curves of sample A at 300 K. The magnetic field was applied along the LAO[001] in-plane direction, which is parallel to the easy magnetization axis (c-axis) of $L1_0$-FeNi(110)/LAO(110). The H_c value in this direction ($H_{c,1}$) is 319 kA/m, which is higher than that of as-deposited sample A before the NITE process (37 kA/m), as listed in Table 2, and the reported randomly oriented $L1_0$-FeNi film (159 kA/m) [23]. The improvement in S after the NITE process, as well as the resulting uniaxial orientation, led to a large $H_{c,1}$. The slight reduction in saturation magnetization (M_s) after NITE resulted from the formation of the oxide layer, which was generated by exposure to air after the denitriding process [23]. Further, the magnetization curve showed a two-step magnetization reversal along the LAO[001] in-plane direction. We presume that the magnetization reversal observed in the initial stage arises from the existence of a soft magnetic A1-FeNi component in a low S region and the surface oxide layer. The H_c values for the magnetic field along the LAO[1$\bar{1}$0] in-plane ($H_{c,2}$) and out-of-plane directions were 63 and 53 kA/m, respectively, confirming the presence of magnetic anisotropy. Fig. 6(b) shows the magnetization curves measured at 10 K. As a result of a reduction in thermal fluctuations, the $H_{c,1}$ value increased to 358 kA/m.

In-plane magnetic torque measurements at 300 K were performed to evaluate the K_u values of the films. Fig. 6(c) shows the torque per unit of volume (L) of the samples A-C as a function of the angle θ_L between the external magnetic field and the easy magnetization axis, assuming a uniaxial magnetic anisotropy. The magnetic anisotropy energy (E_a) is given by $E_a \sim K_u \sin^2\theta_L$ [28)29)] and the $L(\theta_L)$ value is given using

$$L(\theta_L) = -\frac{\partial E_a}{\partial \theta_L} \sim -K_u \sin 2\theta_L. \quad (4)$$

The experimental torque data fit the sinusoidal function given by Eq. (4) well, indicating a uniaxial magnetic anisotropy of the film. From the fitting, the K_u value of sample A is estimated to be 0.63 ± 0.07 MJ/m^3. This value is reasonable because it is close to the theoretically predicted value (K_u = 0.58-0.7 at S = 0.75)[30)31)]. The same analyses were performed for samples B and C, and the results are summarized in Table 2.

The $H_{c,1}$ versus K_u plot of the samples A-C is shown in Fig. 5(d) to investigate the relationship between these two parameters. Here, H_c was calculated from K_u using [28)32)]

$$H_c = \alpha \frac{2K_u}{\mu_0 M_s} - N_{eff} M_s, \quad (5)$$

Table 2 M_s, H_c, and K_u of the samples A–C measured at 300 K. $H_{c,1}$ and $H_{c,2}$ denote the coercivities along the LAO[001] and LAO[1$\bar{1}$0] in-plane directions, respectively. As references, the results for as-deposited samples of A and B are also shown

	M_s [kA/m]	$H_{c,1}$ [kA/m]	$H_{c,2}$ [kA/m]	K_u [MJ/m^3]
Sample A	1077	319	63	0.63
Sample B	1073	209	58	0.39
Sample C	1059	159	77	0.35
Sample A (as-deposited)	1117	37	42	-
Sample B (as-deposited)	1219	36	39	-

where μ_0, α, and N_{eff} represent the vacuum permeability, Kronmüller factor, and effective demagnetization factor, respectively. The first and second terms in the right side of Eq. (5) relate to an anisotropy and demagnetization fields, respectively. The value of α depends on the density of defects and inhomogeneous nanostructures that act as nucleation points of magnetization reversal in the material. If ideal SW-type particles are achieved, α is equal to 1 [21)]. A linear fitting for the plot in Fig. 5(d) was performed using Eq. (5) with the average M_s (1070 kA/m) of samples A-C, giving α = 0.34 and N_{eff} = 0.01. This α is lower than that expected for SW-type particles, and the reduction can be attributed to imperfections in the island structures and surface oxide layers because it has been reported that α ranges from 0.2 to 0.4 for practical magnetic materials [32)]. When N_{eff} is zero in continuous films parallel to the plane direction [28], the small N_{eff} implies that the films are nearly continuous because the flat islands are partially connected and/or magnetically interacted because of the narrow gaps between them. To improve H_c values further, precise morphological control such as by using lithography is required to form isolated islands. For thick films (e.g., sample B), a reduction in K_u was observed despite the high S. The possible reasons are the presence of a small amount of soft magnetic nitrogen residues [23)], as well as the influence of grain boundaries and anti-phase boundaries [20)]. It is necessary to clarify the origin of the reduction and take measures to minimize them for improving the K_u values further.

4. CONCLUSIONS

$L1_0$-FeNi thin films with island structures showing uniaxial magnetic anisotropy were prepared by sputter depositing FeNi thin films onto LAO(110) substrates and applying NITE. The film with an S of 0.74 exhibited magnetic properties with uniaxial orientation in the film plane, yielding a K_u of 0.63 MJ/m^3 at 300 K, and H_c of 319 and 358 kA/m at 300 and 10 K, respectively, which is the highest H_c of an artificial $L1_0$-FeNi system reported to date. The highest H_c value is primarily responsible for the uniaxial orientation in the $L1_0$-FeNi film with an island structure that can be considered as the SW-type particles. To increase H_c and K_u values further, it is necessary to control the morphology of the films and to elucidate the relationship between the magnetic properties and local microstructures such as soft magnetic nitrogen residues, grain boundaries, and anti-phase boundaries.

5. Acknowledgements

This study was supported by the Future Pioneering Program“Development of magnetic material technology for high-efficiency motors”(Proposal No. JPNP14015) commissioned by the New Energy and Industrial Technology Development Organization (NEDO), Japan.

References

1) J. Cui, M. Kramer, L. Zhou, F. Liu, A. Gabay, G. Hadjipanayis, B. Balasubramanian, D. Sellmyer, Current progress and future challenges in rare-earth-free permanent magnets, Acta Mater. 158 (2018) 118-137.
2) A. Hirohata, H. Sukegawa, H. Yanagihara, I. Zutic, T. Seki, S. Mizukami, R. Swaminathan, Roadmap for emerging materials for spintronic device applications, IEEE Trans. Magn. 51 (2015) 1-11.
3) K. Takanashi, M. Mizuguchi, T. Kojima, T. Tashiro, Fabrication and characterization of $L1_0$-ordered FeNi thin films, J. Phys. D. Appl. Phys. 50 (2017) 483002.
4) M. Kotsugi, M. Mizuguchi, S. Sekiya, M. Mizumaki, T. Kojima, T. Nakamura, H. Osawa, K. Kodama, T. Ohtsuki, T. Ohkochi, K. Takanashi, and Y. Watanabe, Origin of strong magnetic anisotropy in $L1_0$-FeNi probed by angular-dependent magnetic circular dichroism, J. Magn. Magn. Mater. 326 (2013) 235-239.
5) Y. Miura, S. Ozaki, Y. Kuwahara, M. Tsujikawa, K. Abe, and M. Shirai, The origin of perpendicular magneto-crystalline anisotropy in $L1_0$–FeNi under tetragonal distortion, J. Phys. Condens. Matter. 25 (2013) 106005.
6) E. Poirier, F.E. Pinkerton, R. Kubic, R.K. Mishra, N. Bordeaux, A. Mubarok, L.H. Lewis, J.I. Goldstein, R. Skomski, K. Barmak, Intrinsic magnetic properties of $L1_0$-FeNi obtained from meteorite NWA 6259, J. Appl. Phys. 117 (2015) 17E318.
7) M. Kotsugi, C. Mitsumata, H. Maruyama, T. Wakita, T. Taniuchi, K. Ono, M. Suzuki, N. Kawamura, N. Ishimatsu, M. Oshima, O. Watanabe, M. Taniguchi, Novel magnetic domain structure in iron meteorite induced by the presence of $L1_0$-FeNi, Appl. Phys. Express. 3 (2010) 13001.
8) T. Nagata, J. Danon, M. Funaki, Magnetic properties of Ni-rich iron meteorites, Mem. Natl. Inst. Polar Res., Spec. Issue 46 (1987) 263-282.
9) M. Uehara, J. Gattacceca, H. Leroux, D. Jacob, C.J. Van Der Beek, Magnetic microstructures of metal grains in equilibrated ordinary chondrites and implications for paleomagnetism of meteorites, Earth Planet. Sci. Lett. 306 (2011) 241-252.
10) L. Néel, J. Pauleve, R. Pauthenet, J. Laugier, D. Dautreppe, Magnetic properties of an iron–nickel single crystal ordered by neutron bombardment, J. Appl. Phys. 35 (1964) 873-876.
11) J. Paulevé, A. Chamberod, K. Krebs, A. Bourret, Magnetization curves of FeNi (50-50) single crystals ordered by neutron irradiation with an applied magnetic field, J. Appl. Phys. 39 (1968) 989-990.
12) R.J. Arnott, A. Wold, The preparation and crystallography of FeNiN and the series Fe4-xNixN, J. Phys. Chem. Solids. 15 (1960) 152-156.
13) S. Goto, H. Kura, H. Yanagihara, E. Kita, M. Tsujikawa, R. Sasaki, M. Shirai, Y. Kobayashi, T. Honda, K. Ono, Positive Weiss temperature in layered antiferromagnetic FeNiN for high-performance permanent magnets, ACS Appl. Nano Mater. 2 (2019) 6909-6917.
14) S. Goto, H. Kura, E. Watanabe, Y. Hayashi, H. Yanagihara, Y. Shimada, M. Mizuguchi, K. Takanashi, E. Kita, Synthesis of single-phase $L1_0$-FeNi magnet powder by nitrogen insertion and topotactic extraction, Sci. Rep. 7 (2017) 13216.
15) S. Mandal, A. Panigrahi, A. Rath, M. Bönisch, P. Sengupta, M. Debata, S. Basu, Formation of L10 ordering in FeNi by mechanical alloying and field-assisted heat treatment: Synchrotron XRD studies, ACS Omega 8 (2023) 13690-13701.
16) Y.P. Ivanov, B. Sarac, S. V. Ketov, J. Eckert, A.L. Greer, Direct formation of hard-magnetic tetrataenite in bulk alloy castings, Adv. Sci. 10 (2023) e2204315–e2204315.
17) T. Kojima, M. Ogiwara, M. Mizuguchi, M. Kotsugi, T. Koganezawa, T. Ohtsuki, T.Y. Tashiro, K. Takanashi, Fe-Ni composition dependence of magnetic anisotropy in artificially fabricated L10-ordered FeNi films, J. Phys. Condens. Matter 26 (2014) 64207.
18) K. Ito, M. Hayashida, M. Mizuguchi, T. Suemasu, H. Yanagihara, K. Takanashi, Fabrication of $L1_0$-FeNi films by denitriding FeNiN films, J. Magn. Soc. Jpn. 43 (2019) 79-83.
19) K. Ito, M. Hayashida, H. Masuda, T. Nishio, S. Goto, H. Kura, T. Koganezawa, M. Mizuguchi, Y. Shimada, T.J. Konno, H. Yanagihara, K. Takanashi, Epitaxial $L1_0$-FeNi films with high degree of order and large uniaxial magnetic anisotropy fabricated by denitriding FeNiN films, Appl. Phys. Lett. 116 (2020) 242404.
20) K. Ito, T. Ichimura, M. Hayashida, T. Nishio, S. Goto, H. Kura, R. Sasaki, M. Tsujikawa, M. Shirai, T. Koganezawa, M. Mizuguchi, Y. Shimada, T.J. Konno, H. Yanagihara, K. Takanashi, Fabrication of $L1_0$-ordered FeNi films by denitriding FeNiN(001) and FeNiN(110) films, J. Alloys Compd. 946 (2023) 169450.
21) E.C. Stoner, E.P. Wohlfarth, A mechanism of magnetic hysteresis in heterogeneous alloys, Philos. Trans. Royal Soc. A 240 (1948) 599-642.
22) T.Y. Tashiro, M. Mizuguchi, T. Kojima, T. Koganezawa, M. Kotsugi, T. Ohtsuki, K. Takanashi, Structural and magnetic properties of FeNi thin films fabricated on amorphous substrates, J. Appl. Phys. 117, 17E309 (2015).
23) T. Nishio, H. Kura, K. Ito, K. Takanashi, H. Yanagihara, Fabrication of $L1_0$-FeNi films with island structures by nitrogen insertion and topotactic extraction for improved coercivity, APL Mater. 9 (2021).
24) Y. Seto, M. Ohtsuka, ReciPro: Free and open-source multipurpose crystallographic software integrating a crystal model database and viewer, diffraction and microscopy simulators, and diffraction data analysis tools, J. Appl. Crystallogr. 55 (2022) 397-410.
25) K. Momma, F. Izumi, VESTA 3 for three-dimensional visualization of crystal, volumetric and morphology data, J. Appl. Crystallogr. 44 (2011) 1272-1276.
26) A. Nakatsuka, O. Ohtaka, H. Arima, N. Nakayama, T. Mizota, Cubic phase of single-crystal $LaAlO_3$ perovskite synthesized at 4.5 GPa and 1273 K, Acta Crystallogr. Sect. E Struct. Rep. Online 61 (2005) i148-i150.
27) S. Goto, H. Kura, M. Tsujikawa, M. Shirai, K. Ito, T. Suemasu, K. Takanashi, H. Yanagihara, Synthesis and magnetic properties of tetragonally ordered Fe_2Ni_2N alloy using topotactic nitriding reaction, J. Alloys Compd. 885 (2021) 161122.
28) J.M.D. Coey, Magnetism and magnetic materials, Cambridge University Press, 9780521816144 (2010) 1-617.
29) S. Chikazumi, Physics of Ferromagnetism, 2nd ed., Oxford University Press, New York, 2009.
30) A. Izardar, C. Ederer, Interplay between chemical order and magnetic properties in $L1_0$-FeNi (tetrataenite): A first-principles study, Phys. Rev. Mater. 4 (2020) 054418.
31) Z. Qiao, M. Tsujikawa, M. Shirai, The effect of chemical disorder on magnetic properties of FeNi and Fe_2Ni_2N alloys, J. Magn. Magn. Mater. 568 (2023) 170362.
32) H. Kronmüller, Theory of nucleation fields in inhomogeneous ferromagnets, Phys. Status Solidi 144 (1987) 385-396.

特集

著者

西尾 隆宏
にしお たかひろ
マテリアル研究部　博士（工学）
機能材料の開発や分析に従事

伊藤 啓太
いとう けいた
東北大学金属材料研究所　博士（工学）
磁性窒化物薄膜材料の開発に従事

藏 裕彰
くら ひろあき
材料技術部　博士（工学）
磁性材料の研究開発に従事

高梨 弘毅
たかなし こうき
東北大学 金属材料研究所
（現所属：日本原子力研究開発機構 先端基礎研究センター）　理学博士
磁性材料・スピントロニクスの研究開発に従事

柳原 英人
やなぎはら ひでと
筑波大学数理物質系　博士（工学）
磁性薄膜の研究および磁気評価手法の開発に従事